Front. Chem. Sci. Eng. 2023, 17(7): 893–905
https://doi.org/10.1007/s11705-022-2290-8

RESEARCH ARTICLE

Nanosilver anchored alginate/poly(acrylic acid/acrylamide) double-network hydrogel composites for efficient catalytic degradation of organic dyes

Fan Zhang, Ce Gao (✉), Shang-Ru Zhai, Qing-Da An (✉)

Liaoning Key Lab of Lignocellulose Chemistry and BioMaterials, Liaoning Collaborative Innovation Center for Lignocellulosic Biorefinery, College of Light Industry and Chemical Engineering, Dalian Polytechnic University, Dalian 116034, China

Abstract A novel alginate/poly(acrylic acid/acrylamide) double-network hydrogel composite with silver nanoparticles was successfully fabricated using the sol–gel method. The presence of carboxyl and amide groups in the network structure provided abundant active sites for complexing silver ions, facilitating the *in situ* reduction and confinement of silver nanoparticles. In batch experiments, the optimal silver loading was 20%, and 5 mmol·L^{-1} of *p*-nitrophenol was completely degraded in 113 s with a rate constant value of 4.057×10^{-2} s^{-1}. In the tap water system and simulated seawater system, the degradation time of *p*-nitrophenol at the same concentration was 261 and 276 s, respectively, with a conversion rate above 99%. In the fixed-bed experiment, the conversion rate remained above 74% after 3 h at a flowing rate of 7 mL·min^{-1}. After 8 cycling tests, the conversion rate remained at 98.7%. Moreover, the catalyst exhibited outstanding performance in the degradation experiment of four typical organic dyes.

Keywords double-network hydrogel, dye degradation, silver nanoparticles, alginate

1 Introduction

Nowadays, the management of organic dye water pollution has become one of the most urgent problems. Most organic dyes, including *p*-nitrophenol (4-NP), rhodamine B (RhB), methylene blue (MB), and methyl orange (MO), are toxic, water-soluble, and non-biodegradable, which makes their removal challenging [1]. Among them, 4-NP is the most representative organic dye widely used in textile, leather, pesticide, and other fields. The methods that have been developed for the removal of organic dyes include efficiency adsorption, photocatalytic degradation, catalytic degradation, and advanced oxidation [2–4].

Due to surface and interface effects, quantum size effects, and macroscopic quantum tunneling effects [5], nanomaterials have recently shown mechanical, optical, electrical, and magnetic advantages over conventional materials. It has become a hot spot in numerous fields, including catalysis, sensing, energy storage, medicine, and agriculture [6–10]. Large surface area and abundant surface active sites are advantages of metal nanoparticles (NPs). They exhibit excellent activity and selectivity in catalytic reactions such as reduction, oxidation, and cracking. With these benefits, the reaction efficiency increased, and activation energy decreased [11]. On the other hand, metal NPs tend to combine quickly because of their high surface energy during preparation, which is a barrier to improving catalytic effectiveness. More importantly, the effect of nanoscale size made it difficult to recover metal NPs. In response to these disadvantages, catalyst carriers show good control over the size and dispersion of metal NPs. For example, Jia et al. [12] prepared Cu/Cu$_x$O @CN copper-based catalyst with small volume and high dispersion by the pyrolysis method. The large specific surface area and sufficient defect points are beneficial for controlling the growth and dispersion of Cu/Cu$_x$O NPs, but the conversion rate decreased after six repetitions.

The recovery operation is another crucial concern for catalysts, significantly affecting maintenance time and catalytic efficiency. Complicated processes also lead to secondary pollution and increased costs. To increase recycling effectiveness, the development of hydrogel catalysts has received much attention [13–15]. Shah et al. [16] synthesized a multiresponsive tercopolymer microgel by free radical emulsion polymerization, which could accomplish the catalytic degradation of 4-NP, Congo red, and MB. The catalyst did not lose its catalytic performance

Received October 7, 2022; accepted December 9, 2022

E-mails: gaoce@dlpu.edu.cn (Gao C.), anqingda@dlpu.edu.cn (An Q.)

after five uses. Wang et al. [17] successfully prepared silver nanoparticle-loaded nanofibrous hydrogel. The size of silver NPs was effectively controlled within 5 nm. It showed good catalytic activity in the reduction of 4-nitrothiophene to 4-aminothiophene in the catalytic reaction. More importantly, the catalyst was easily recovered, and its catalytic activity was not lost after four recoveries. It is noteworthy that the preparation of a hydrogel catalyst was a correct strategy. It effectively controlled the size and distribution of metal NPs and significantly improved the recovery and service life of the catalyst. Based on the requirement of green chemistry, one of the urgent issues that scientific researchers need to solve is developing of a hydrogel carrier material with a simple preparation procedure, high efficiency, stability, and environment-friendly characteristics.

Double-network (DN) hydrogels have been an emerging concept in recent years. They refer to hydrogel materials composed of two intertwined cross-linked networks. It has been rapidly evolving as a new category of intelligent soft materials, and many scholar are continually researching the potential uses of DN hydrogels. This hydrogel has more pronounced advantages over conventional hydrogel materials, including excellent mechanical properties exceptional biocompatibility, and significant strength [18]. Therefore, it is frequently used in drug delivery, tissue engineering, sensing devices, energy storage, and water treatment [19–21]. Wu et al. [22] used a one-pot approach to create DN nanocomposite hydrogel catalysts with excellent photocatalytic degradation of MB. The results indicated that selecting DN hydrogel as the medium to carry metal NPs was a sensible decision.

Biomaterials provide advantages over other materials, such as abundant storage, low cost, and renewable energy. Therefore, developing applications of biomaterials and maximizing the use of renewable resources are of great significance in solving the resource crisis. It has been determined that biomass resources, including sodium alginate (SA), lignin, chitosan, and carboxymethylcellulose sodium, can be employed to create functionalized hydrogel materials [23]. Our research team previously worked on the research and development of biomass materials for multifunctional applications, particularly the controllable synthesis of hydrogel substrate materials based on SA [24]. A natural seaweed polysaccharide called SA is composed of M units (–D-mannuronic) and G units (–L-guluronic) connected by β-1,4 glycosidic linkages. The G segment contains a large number of carboxylates, which chelates with divalent or trivalent metals to create a hydrogel material with a three-dimensional network. Furthermore, traditional ionic alginate-based hydrogels are composed of rigid networks with medium stability. We developed a new method for synthesizing alginate-based hydrogel substrates. The concept of DN hydrogel was used to further improve catalytic efficiency and limit active components to satisfy the design requirements of catalysts. Simple two-step crosslinking techniques were used to construct multifunctional alginate/poly(acrylic acid/acrylamide) (PAA/PAM) DN hydrogel (SPDH) composites. Acrylic acid (AA) and acrylamide (AM) were chosen as raw materials for the following reasons: The addition of AA and AM causes abundant synthetic hydrogel materials in carboxyl and amide groups, and the addition of electron-rich groups gives metal ions more complexation sites and prevents the aggregation of metal NPs [25]. The silver-based catalyst was synthesized by direct *in situ* reduction using silver NPs as a research object, which considered both the catalytic efficiency and the cost-effectiveness. To examine the degradation performance of SPDH@Ag combination material, 4-NP was selected as the model pollutant to analyze the catalytic efficiency in static batch tests, fixed bed studies, and reusability experiments. In addition, a multi-dye degradation system was also investigated in this study.

2 Experimental

2.1 Materials and methods

AA (AR, > 99%, GC), AM (AR, 99%), and RhB (AR) were bought from Shanghai Macklin Biological Co., Ltd., China. MO (AR, 99%) and SA (AR, 98%, viscosity range: 1.05–1.15 Pa·s, Table S1, cf. Electronic Supplementary Material, ESM) were provided by Tianjin Guangfu Fine Chemical Research Institute. MB (AR, ⩾ 82.0%) and ammonium persulfate (APS, AR) were obtained from Sinopharm Chemical Reagent Co., Ltd. $AgNO_3$ (AR, ⩾ 99.8%), Na_2SO_4 (AR), NaCl (AR, 99.5%), $CaCl_2$ (AR), and KCl (AR) were purchased from Tianjin Kermel Chemical Reagent Co., Ltd., China. $MgCl_2$, (AR, ⩾ 98.0%) was provided by Tianjin Guangfu Fine Chemical Reagent Co., Ltd., China. $NaBH_4$ (AR, 98%), 4-NP (AR, > 99.0%), and Ponceau S (PS, AR, 99%) were all provided by Shandong Xiya Chemical Reagent Co., Ltd., China. Deionized water was obtained from laboratory deionization equipment. The chemical reagents used in the experiment were used directly without purification.

2.2 Sample preparation method

2.2.1 Preparation of SPDH composites

A novel two-step sol–gel crosslinking process was designed to prepare SPDH composites, and the DN hydrogel was easily fabricated. Scheme 1 demonstrates the preparation process. Deionized water was used to dissolve SA to provide a consistently clear solution (1%, w/v). In a reaction container, 4.5 g of SA solution and 2 mL of AA were well combined and stirred for 30 min. Then, 2 g of AM and 1 mL of deionized water were

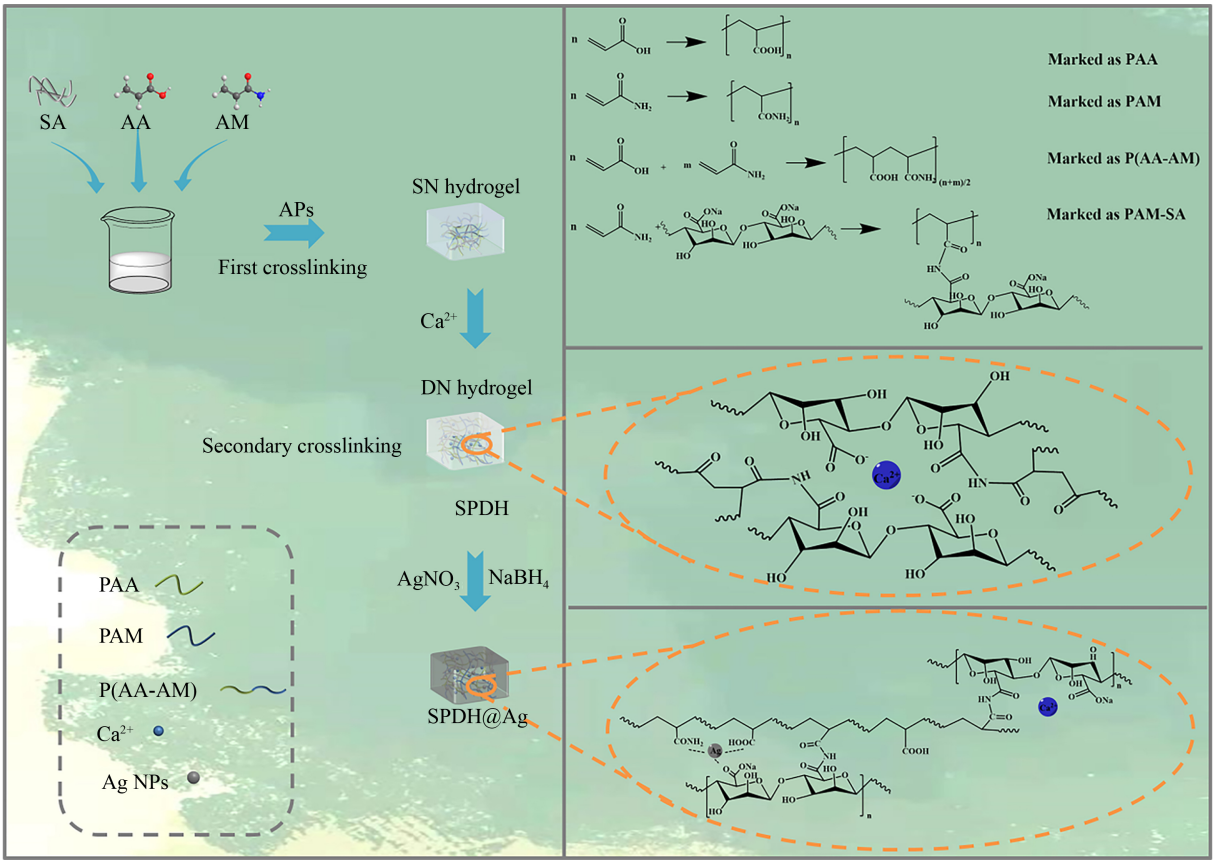

Scheme 1 The preparation flow chart of SPDH@Ag.

added to the reaction system one at a time and mixed until well dissolved. The final step was to add 0.1 g of APS. To create clear single-network (SN) hydrogel, the mixture underwent ultrasonic treatment for 15 min before being heated in a water bath at 50 °C for 90 min. After immersing it in $CaCl_2$ (5 wt %) aqueous solution for 6 h, the DN hydrogel was fabricated. After washing with enough deionized water and ethanol solution (CH_3CH_2OH: H_2O = 7:3), the SPDH composite was obtained.

2.2.2 Preparation of SPDH@Ag catalyst

The preparation method of SPDH@Ag was simple and the preparation process was illustrated in Scheme 1. First, 100 mg of SPDH was immersed in $AgNO_3$ solution (0.185 mmol $AgNO_3$ in 5 mL H_2O) and placed in a dark environment for 12 h. $NaBH_4$ solution (5 mL, 200 mg·L^{-1}) was added into the system and react for 2 h. After that, SPDH@Ag-20 was washed alternately with deionized water and ethanol until there was no residue. After preserving at –50 °C overnight, the lyophilizer was used to remove residual water. In addition, to get SPDH@Ag with different silver loading capacities, several amounts of $AgNO_3$ (0.0463, 0.0927, 0.139, and 0.232 mmol) were used in the preparation procedure, which were labeled as SPDH@Ag-5, SPDH@Ag-10, SPDH@Ag-15, and SPDH @Ag-25, respectively.

2.3 Catalytic performance test

2.3.1 Batch experiment operation

2.3.1.1 Catalytic degradation of 4-NP

To measure the catalytic efficiency of SPDH@Ag, we carried out 4-NP hydrogenation reduction to test catalytic efficiency. Fresh $NaBH_4$ solution (0.2 mol·L^{-1}) and 4-NP solution (5 mmol·L^{-1}) were prepared before the experiment. The entire reaction system was completely exposed to a nitrogen atmosphere. SPDH@Ag (100 mg) and 4-NP solution (10 mL) were transferred into a three-necked flask. After injecting 15 mL $NaBH_4$ solution, reacting solution was periodically taken out from reactor, and the absorbance of 4-NP was measured by using ultraviolet–visible (UV–vis) absorption spectroscopy with the range from 200 to 800 nm.

2.3.1.2 Catalytic degradation of 4-NP in different water systems

Besides the deionized water system, the reduction experiment of 4-NP in the tap water system and the simulated seawater system were also carried out to study whether the complex water environment affected the catalytic performance. The difference from the above experiment

was that the tap water directly obtained from the laboratory (without any treatment) and the simulated seawater prepared in advance (the specific information is shown in Table S2, cf. ESM) were used instead of deionized water when preparing the 4-NP solution. For detailed experimental steps, please refer to Section 2.3.1.1.

2.3.1.3 Catalytic reduction of organic dyes

More importantly, SPDH@Ag was also used for the degradation experiment of organic dyes. Here, MO, MB, RhB, and PS were chosen as representatives of organic dyes for catalytic testing. Fresh $NaBH_4$ solution (0.2 $mol \cdot L^{-1}$) and dye solution solution (500 $mg \cdot L^{-1}$) were prepared in advance. The specific experimental steps refer to 2.3.1.1. The entire experimental reaction process was still monitored using UV–vis absorption spectroscopy.

2.3.2 Fixed-bed experiment under the dynamical condition

The macroscopic volume is the advantage of SPDH@Ag, which can exist stably in the catalytic experimental environment while effectively reducing the loss of active components. Therefore, fixed-bed experiment was used to research the catalytic property of SPDH@Ag under the dynamic environment. As shown in Scheme 2, 300 mg SPDH@Ag was filled into the reaction column, two peristaltic pumps were used to transfer 4-NP solution (50 $mg \cdot L^{-1}$) and $NaBH_4$ solution (200 $mg \cdot L^{-1}$) from the bottom of the reaction column. The reactant solution from the top of column was collected every 5 min, and residual concentration was measured by UV–vis absorption spectroscopy. In addition, the influence of the distinct velocity with flow rates (3, 5, and 7 $mL \cdot min^{-1}$) was also investigated.

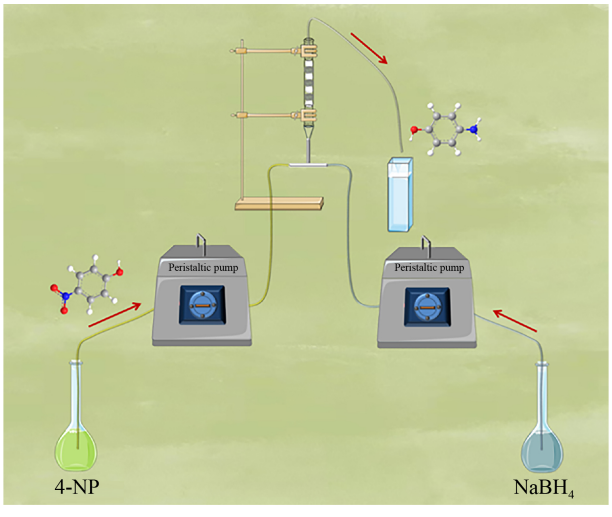

Scheme 2 Diagram of the experimental setup of the 4-NP hydrogenation fixed-bed.

2.3.3 Recyclability and reusability experiment

Recyclability and reusability are also important factors to judge the performance of the catalyst. The specific steps were as follows: $NaBH_4$ solution (0.2 $mol \cdot L^{-1}$) and 4-NP solution (5 $mmol \cdot L^{-1}$) were prepared in advance. 4-NP solution (10 mL), SPDH@Ag (100 mg), and $NaBH_4$ solution (15 mL) were successively added to three-necked flasks, and the reaction solution was taken out regularly and determined by UV–vis absorption spectroscopy. The catalyst was separated from the reaction system through filtration operation after the reaction. Subsequently, the catalyst regeneration step could be completed by alternately washing the recovered catalyst with deionized water and ethanol three times. Next, the regenerated catalyst was applied to the batch experiment of 4-NP, the above operations were repeated 8 times. This process was performed to determine whether the catalytic performance was affected and whether its microstructure could preserve after cycling.

2.4 Sample characterization

The morphology of nanosilver was obtained by transmission electron microscopy (TEM, JEM-2100). The morphology, structure, and element distribution of the samples were obtained by thermal field emission scanning electron microscopy (SEM, JEM-7800F) and energy dispersive X-ray diffractometer (EDS). X-ray diffractometer (XRD-6100, SHIMADZU) was used to record crystal data in the range of 10° to 80° with Cu Kα radiation source, and scanning speed was 2 $(°) \cdot min^{-1}$. The functional group information of the sample was obtained by an infrared spectrometer (Spectrum Two, USA). X-ray photoelectron spectroscopy (XPS, ESCALAB250, Thermal VG) was used to characterize the basic elemental composition of the sample. The catalytic experimental data were all obtained by UV–vis absorption spectroscopy (Agilent Cary 60).

3 Results and discussion

3.1 Materials characterization

As shown in Fig. 1, the microscopic morphology of the composites and the dispersion of the active components were researched by SEM and TEM. Figure 1(a) depicts the microstructure of SPDH. It can be seen that the gel has a three-dimensional network structure with glaring voids and cavity walls. The inset high-resolution SEM (HR-SEM) image shows that the surface of the cavity walls is not smooth but scale-like, which can offer a greater specific surface area for the deposition of silver NPs. Figure 1(b) shows the SEM image of SPDH@Ag-20. After the immobilization of silver NPs, the network

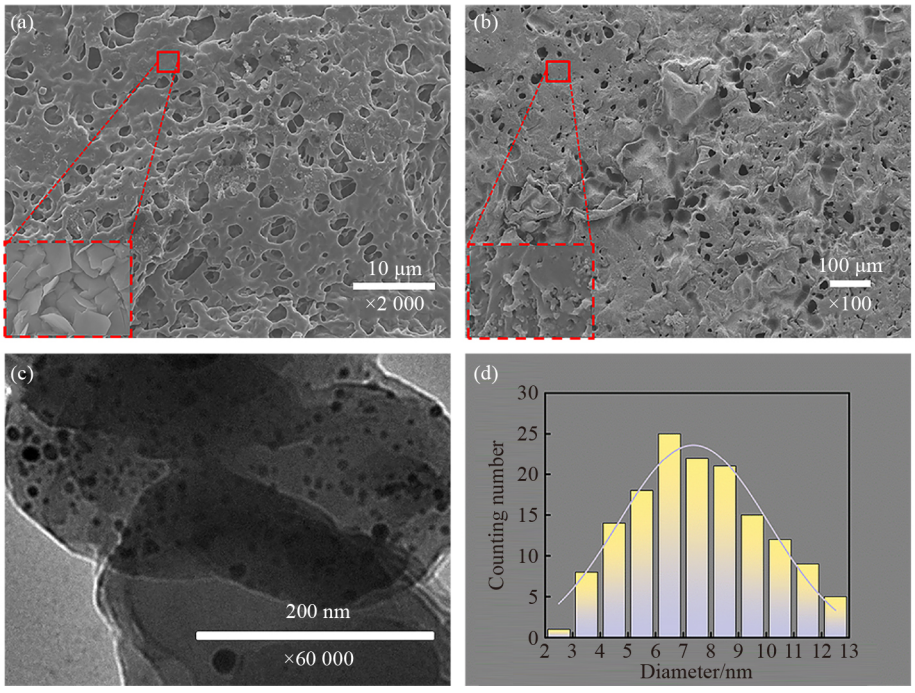

Fig. 1 The images of SEM: (a) SPDH and (b) SPDH@Ag-20; the images of TEM: (c) SPDH@ Ag-20; (d) the diameter dispersion of silver NPs in SPDH@Ag-20.

structure is well maintained without collapse. Similarly, the inset shows an HR-SEM image of the SPDH@Ag-20 cavity wall, where the "scaly" structure still exists compared to SPDH. The morphology and size of Ag NPs on SPDH@Ag-20 were observed by TEM. As shown in Fig. 1(c), the Ag NPs are uniformly dispersed in the structure of carrier material, and the particle size distribution is relatively close. Figure 1(d) summarizes the diameter distribution of the Ag NPs, ranging from 2 to 13 nm, and the average diameter is 7.66 nm. This result indicates that silver ions were successfully introduced into the SPDH and were well complexed by the abundant carboxyl and amide groups and dispersed among the structure. SEM-EDS (Fig. S1, cf. ESM) provides information on the elemental composition and distribution of SPDH@Ag-20. Ag, C, N, O, and Ca elements are detected and uniformly distributed throughout the composites. Table S3 (cf. ESM) summarizes the atomic percentages of C, N, O, Ca, and Ag, which are 46.98%, 14.59%, 29.25%, 0.82%, and 4.70%, respectively. In addition, the element Na is also detected, with an atomic percentage of 3.65%. The source of sodium is presumed to be SA and $NaBH_4$. In summary, the catalysts were successfully synthesized as expected.

XRD was used to characterize SPDH composites with different silver contents and to examine the phase and type of crystals in the synthesized composites. As shown in Fig. 2, there is only one large diffraction peak on the curve of pure SPDH, indicating that it is in an amorphous state and no other metal crystals exist. After the immobilization of the Ag NPs, a clear spike appeared on the XRD curve of the composites. The diffraction peaks at

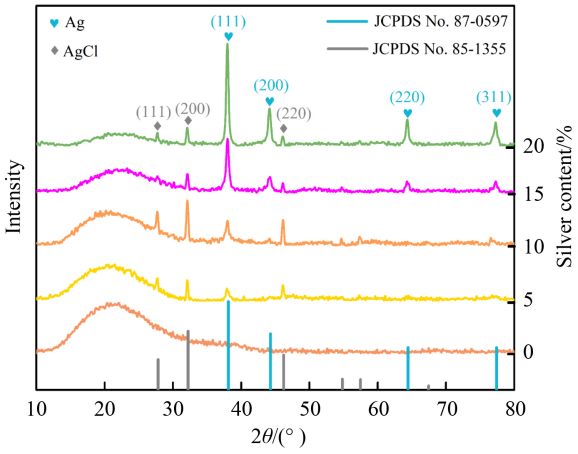

Fig. 2 The XRD patterns of SPDH@Ag with different silver content.

$2\theta = 38.114°$, 44.298°, 64.441°, and 77.395° represent the (111), (200), (220), and (311) crystal planes of elemental silver, respectively, which are in perfect agreement with the results recorded on the PDF card (JCPDS No. 87-0597) [26]. Moreover, the intensity of the four diffraction peaks increases with increasing silver content. In addition, diffraction peaks also appear at 27.824°, 32.237°, and 46.236°, which can be attributed to the (111), (200), and (220) crystal planes of AgCl crystals, respectively (JCPDS No. 85-1355) [27]. This phenomenon is attributed to the residual $CaCl_2$.

Figure 3 summarizes the relevant information on the Fourier transform infrared spectrometer (FTIR) of SPDH

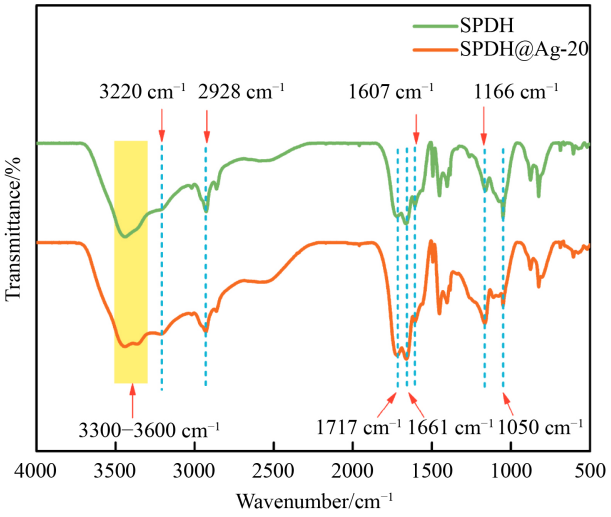

Fig. 3 FTIR results of SPDH and SPDH@Ag-20.

and SPDH@Ag-20. The absorption peak at 3300–3600 cm^{-1} is attributed to the stretching vibration of the N–H bond of the amide [28]. The absorption peak at 3220 cm^{-1} reflects the stretching vibration of –OH of carboxylic acid. The absorption peak at 2928 cm^{-1} indicates the symmetric stretching vibration of $–CH_2$ [29]. The absorption peak at 1717 cm^{-1} is the stretching vibration of C=O on carboxylic acid [30]. Similarly, the absorption peak at 1661 cm^{-1} denotes the stretching vibration of C=O on amide. The absorption peak at 1607 cm^{-1} suggests the N–H bending vibration of the amide. The absorption peaks at 1166 and 1050 cm^{-1} indicate the stretching and bending vibrations of C–N, respectively. Compared to the FTIR curves of the two composites, no new peaks were generated, or old peaks disappeared after the immobilization of immobilizing Ag NPs, indicating that the microstructure of SPDH was stable.

The elemental distribution of SPDH@Ag-20 was characterized by XPS, and the results are shown in Fig. 4. Figure 4(a) shows the XPS data analysis results of SPDH@Ag-20. The main signals captured are C, N, O, Ca, and Ag. As shown in Fig. 4(b), the characteristic peaks at the binding energies of 374.2 and 368.2 eV correspond to Ag $3d_{3/2}$ and Ag $3d_{5/2}$, respectively. This result proves that the SPDH could successfully capture Ag^+ in solution, and Ag NPs were formed *in situ* by the reduction of $NaBH_4$, consistent with the XRD and SEM-EDS results. For the XPS spectrum of C 1s (Fig. 4(c)), different chemical states of carbon elements were detected. The characteristic peaks at 284.3, 285.1, 287.7, and 288.3 eV correspond to C–C, C–O/C–N, C=O, and O=C–O, respectively [31]. As shown in Fig. 4(d), there is only one characteristic peak in the XPS spectrum of N 1s, and the characteristic peak at the binding energy of 399.5 eV corresponds to the signal of $–NH_2$ [32]. Figure 4(e) is the XPS spectrum of O 1s. There are three deconvolution peaks at 531.1, 532.1, and 533.6 eV, representing the signals of C–OH, C–O, and O=C–O, respectively. As shown in Fig. 4(f), the signal of Ca $2p_{1/2}$ and Ca $2p_{3/2}$ appear at binding energies of 350.6 and 347 eV [33], respectively, demonstrating the existence of the calcium alginate network structure. Moreover, the introduction of Ag NPs does not destroy the ionic network structure.

3.2 Catalysis test results under batch condition

3.2.1 Catalytic results of 4-NP

The UV–vis spectrum throughout the catalytic process is shown in Fig. S2 (cf. ESM), with the 4-NP aqueous solution exhibiting a characteristic peak at 317 nm. After mixing with the $NaBH_4$ solution, the characteristic peak is shifted to 400 nm. In addition, the characteristic peak of *p*-aminophenol (4-AP) appears at 300 nm [34].

The catalytic performance of SPDH@Ag with different silver loadings was investigated through batch experiments. The results are presented in Figs. 5 and S3 (cf. ESM). SPDH@Ag-5 required 622 s to finish the reaction, which was the lowest catalytic efficiency due to the insufficient reactive sites for Ag NPs. As the silver loading increases, the time required to complete the catalytic reaction greatly decreases. The reaction times of SPDH@Ag-10, SPDH@Ag-15, SPDH@Ag-20, and SPDH@Ag-25 are 252, 148, 113, and 140 s, respectively. The above results indicate that with the increase of silver loading, more Ag NPs are generated in the network, which served as a reactive site to effectively contact with 4-NP to complete the catalytic reaction. However, when the silver loading increased to 25%, the time to complete the reaction was prolonged, and the presence of silver NPs in the solution after the reaction was observed. Based on the analysis, the optimal silver loading was 20%, and SPDH@Ag-20 was selected for subsequent experiments.

In summary, SPDH@Ag-20 as a catalyst can significantly accelerate the catalytic degradation rate of 4-NP. In the catalytic process, Ag NPs are the active centers with a significant effect with a significant effect. To eliminate the interference factor of the carrier, the following three reaction systems were designed for comparison: (1) 4-NP + $NaBH_4$ system; (2) 4-NP + $NaBH_4$ + SPDH system; (3) 4-NP + $NaBH_4$ + SPDH@Ag-20 system.

In this study, the amount of $NaBH_4$ was far exceeded compared to 4-NP, and the influence was negligible. Therefore, the amount of 4-NP was the main factor affecting the results of the catalytic reaction. The reaction rate constant was calculated using pseudo-first-order kinetic equations:

$$\ln\left(\frac{A_t}{A_0}\right) = \ln\left(\frac{C_t}{C_0}\right) = -kt, \tag{1}$$

$$a = \left(1 - \frac{C_t}{C_0}\right). \tag{2}$$

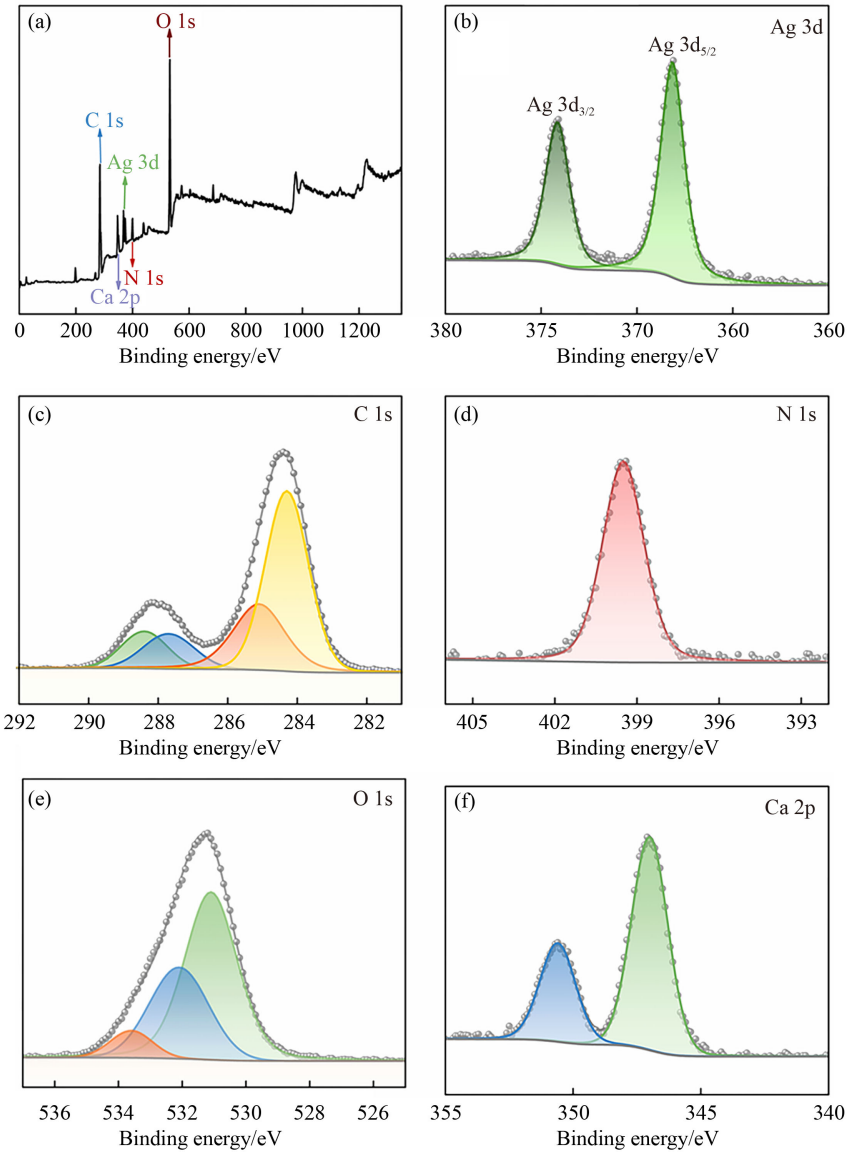

Fig. 4 The XPS results of SPDH@Ag-20: (a) full survey scan spectrum, (b) Ag 3d, (c) C 1s, (d) N 1s, (e) O 1s, and (f) Ca 2p.

In Eq. (1), the reaction rate constant is denoted by k, and t represents the reaction time. A_0 and C_0 are the absorbance and concentration of the reactant at the beginning of the reaction, respectively. Similarly, A_t and C_t represent the absorbance and concentration of the reactant at the reaction time t, respectively. In Eq. (2), a represents the conversion rate and is used to calculate the conversion rate of the reactants. The k value was obtained by calculation and fitting. As shown in Fig. S4 (cf. ESM), the k value is 4.5×10^{-5} s^{-1} in the system without catalysts, indicating that the degradation rate of 4-NP was prolonged. Similarly, the k is only 8.33×10^{-5} s^{-1} in the system with SPDH carrier, indicating that the existence of the carrier barely affected the catalytic process. However, the k of the reaction system with SPDH@Ag-20 is up to 0.04057 s^{-1}. These results suggest that Ag NPs played a significant role in the reaction, accelerating the electron transfer rate and significantly increasing the 4-NP degradation rate.

3.2.2 Catalytic results of 4-NP in different aqueous solutions

The catalytic performance of SPDH@Ag-20 in different water environments was investigated by the degradation experiment of 4-NP in the simulated seawater system and the tap water system. As shown in Fig. 6, the degradation of 4-NP in the simulated seawater system needs 276 s with a k value of 0.01302 s^{-1}. Similarly, the catalytic time of the tap water system is 261 s with a k value of 0.0114 s^{-1}. The results showed that the reaction time was prolonged and the k value was reduced compared with the deionized water system, indicating that the complex water environment reduced the catalytic efficiency to a certain

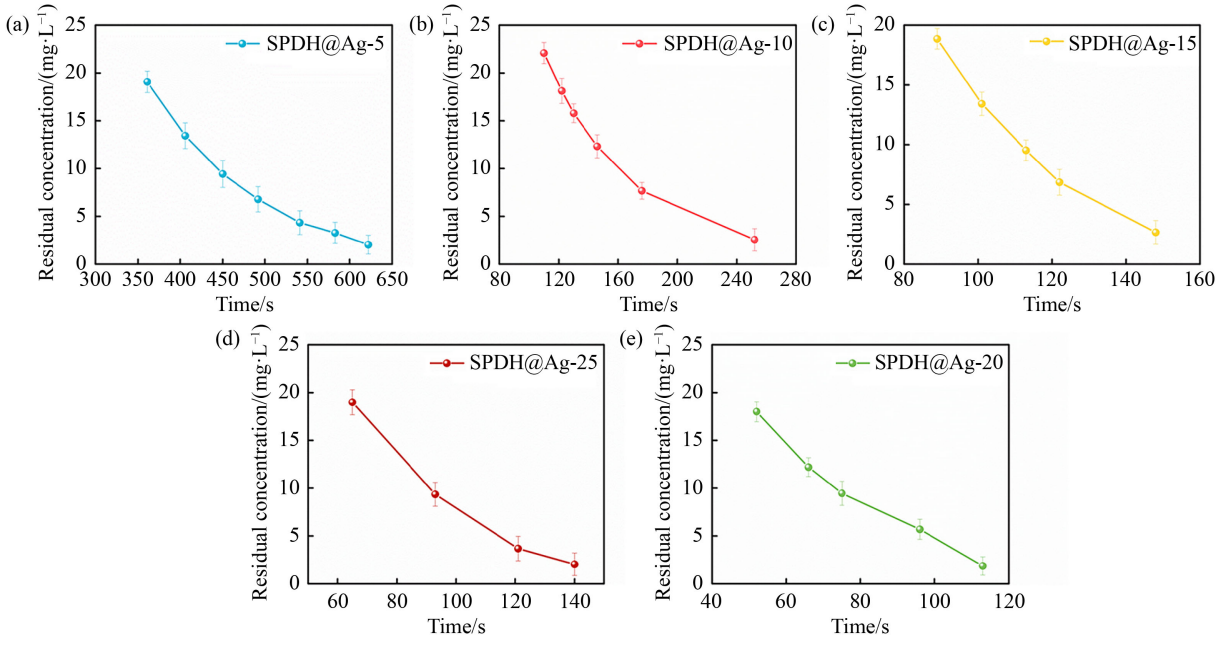

Fig. 5 The results of batch experiment of SPDH@Ag with different silver loads: (a) SPDH@Ag-5, (b) SPDH@Ag-10, (c) SPDH@Ag-15, (d) SPDH@Ag-20, and (e) SPDH@Ag-25.

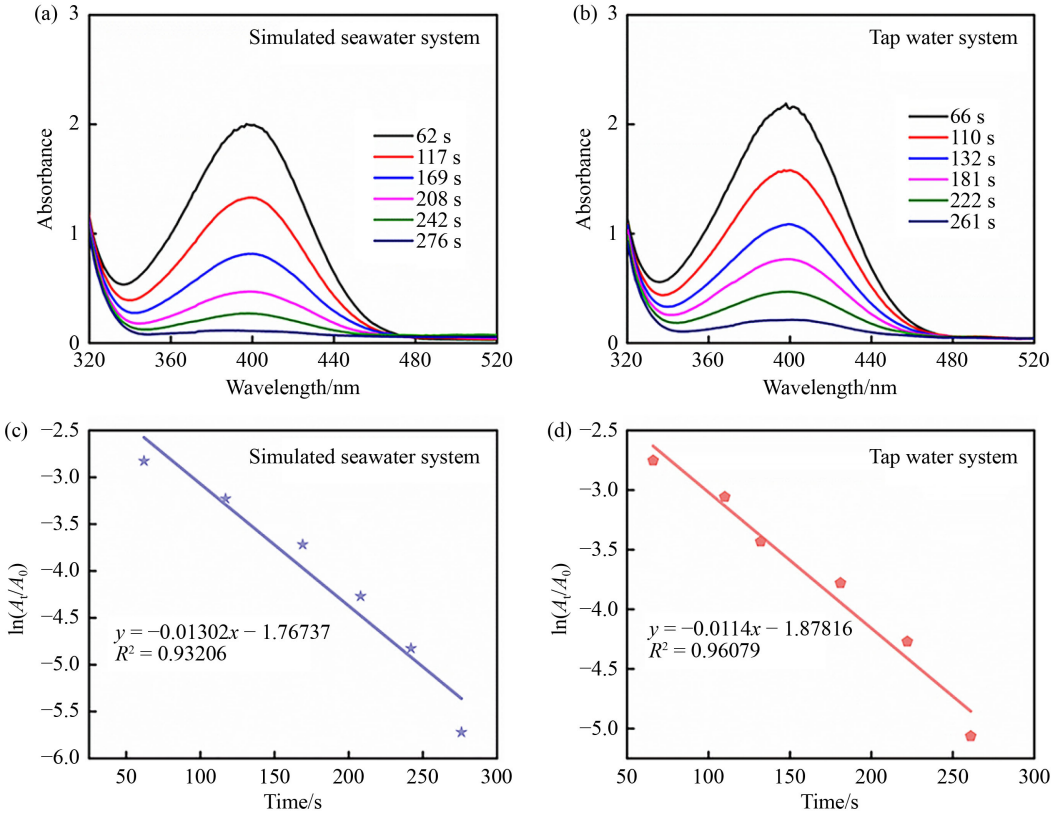

Fig. 6 The UV–vis spectrum of the catalytic process: (a) simulated seawater system and (b) tap water system; the linear fitting: (c) simulated seawater system and (d) tap water system.

extent. Figure 7 summarizes the information related to the residual concentration and conversion of 4-NP in the three solution systems. It can be seen that the conversion efficiency of all three systems exceeds 99%. Despite the interferences of other ions or organic substances in the water environment, the catalytic activity of SPDH@Ag-20 was still efficient. However, the catalytic efficiency is lower in the simulated seawater and tap water systems. It

might be caused by other ions or organic substances, reducing the effective contact of 4-NP molecules with Ag NPs.

3.2.3 Degradation mechanism of 4-NP

Based on the above experimental results, the reduction rate of 4-NP was extremely slow without any catalysts. Conversely, the reaction rate was significantly accelerated with Ag NPs. Therefore, the hydrogenation reduction mechanism of 4-NP is as follows (as shown in Scheme 3): First, the silver-hydrogen complex has a charge-rich surface formed by the adsorption of BH_4^- in the reaction system onto the surface of Ag NPs [35]. Then, 4-NP molecules are also adsorbed on Ag NPs. BH_4^- and 4-NP perform electron transfer on their surfaces and complete the hydrogenation reaction, which is the key step in determining the reaction rate. However, the reaction rates of the simulated seawater and tap water systems are lower than that of the deionized water system due to the coexistence of ions and organics in the two systems, which reduces the effective contact between 4-NP and Ag NPs. Finally, the 4-AP molecules are released from the structural surface of the catalyst into the reaction system. Ag NPs are active sites that provide acceleration of electron transfer between BO_4^- and 4-NP, thus increasing the reaction rate.

3.2.4 Degradation performance for multiple dye system

As shown in Fig. 8, the degradation performance of SPDH@Ag-20 against organic dyes was also explored.

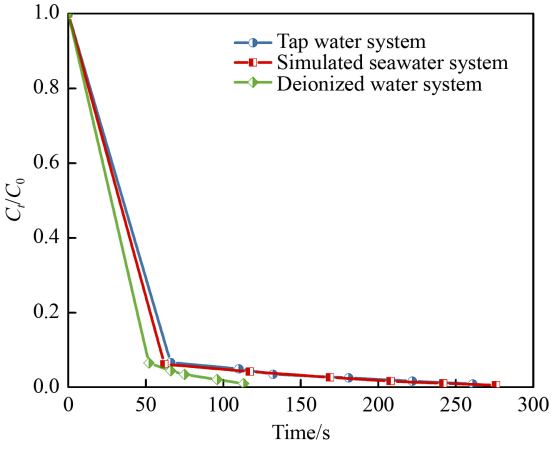

Fig. 7 The relationship between residual ratio and reaction time.

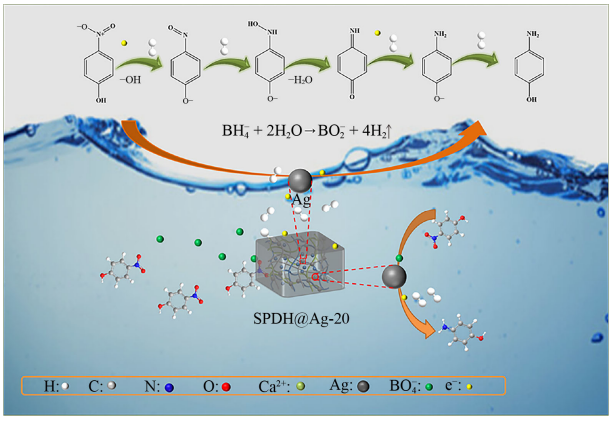

Scheme 3 Reduction mechanism of 4-NP degradation with SPDH@Ag-20.

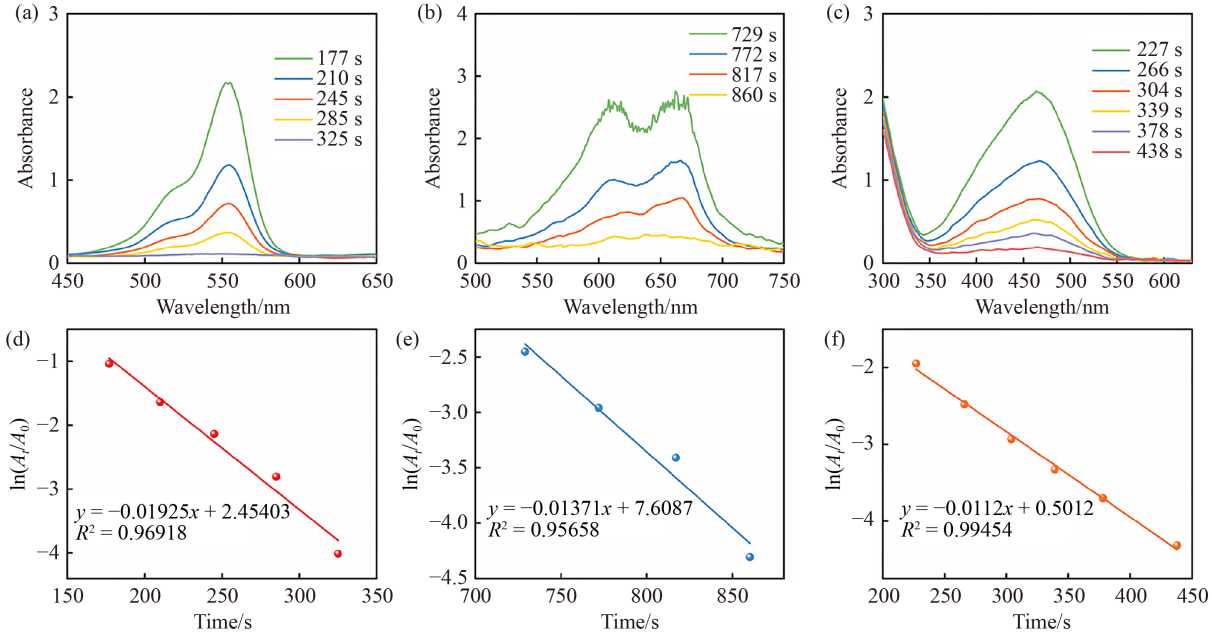

Fig. 8 The UV–vis spectrum of the catalytic process: (a) RhB, (b) MB, and (c) MO; the plots of the $\ln(A_t/A_0)$ vs. reaction time: (d) RhB, (e) MB, and (f) MO.

Figure 8(a) shows the UV–vis curve for the RhB catalytic process, and the characteristic peak appears at 554 nm. When the reaction proceeds to 325 s, the characteristic peak disappears, and the color of the solution system becomes transparent, indicating that the reaction has been completed and the degradation rate (k) of RhB is 0.01925 s^{-1}. The maximum characteristic absorption peak of MB appears at 664 nm (Fig. 8(b)). The characteristic peak disappears after 860 s, and the k value is 0.01371 s^{-1}. As shown in Fig. 8(c), the characteristic peak of MO appears at 464 nm. The characteristic peak disappears after 438 s, with a k value of 0.01112 s^{-1}. Table 1 shows the relevant reports in the same field, and the comparison revealed that SPDH@Ag-20 has excellent catalytic degradation performance for different dyes with fast reaction rates. Figure S5 (cf. ESM) depicts the UV–vis curves of the PS degradation process. Relatively, the catalytic degradation process of the PS is more complex. At the beginning of the reaction, the characteristic peak at 510 nm gradually disappears. The intensity of the peak at 400 nm increases in the initial stage and then gradually decreases, forming the characteristic absorption peak of the intermediate product. This variation is also an important feature of the step-by-step degradation of macromolecular organics. In summary, SPDH@Ag-20 has high catalytic efficiency and extensive degradation performance.

3.3 Catalytic results of the fixed-bed experiment

To better approximate the actual situation, the fixed-bed experiment was carried out to explore the hydrogenation reduction performance of SPDH@Ag-20 for 4-NP under the dynamic environment, and three flowing rates (3, 5, and 7 mL·min^{-1}) were investigated in detail. Figure 9 summarizes the relevant data from the fixed-bed experiment and the residual 4-NP concentrations at different reaction moments. At a flow rate of 3 mL·min^{-1}, the residual concentration is below 3 mg·L^{-1} for 60 min and hardly increases to 7 mg·L^{-1} during the 180 min of catalytic operation. When the flowing rate reaches 5 mL·min^{-1}, the residual concentration is maintained below 10 mg·L^{-1}. When the rate increases to 7 mL·min^{-1}, the catalytic efficiency is not as good as at lower flow rates, with residual concentration below 13 mg·L^{-1} at about 180 min and conversion rate remaining above 74%. From the experimental data, it can be seen that the residual concentration increases as the flow rate increases, which was caused by the short contact time between the reactants and the catalyst and insufficient reaction. These results demonstrate that the SPDH@Ag-20 also exhibited good catalysis function in the fixed-bed experiment.

Table 1 Comparison of the catalytic activity of SPDH@Ag-20 for dyes with previously reported work

Pollutant	Catalyst	C_0/(mmol·L^{-1})	Time/min	k/s^{-1}	Ref.
RhB	PtRh ANMPs	0.3	14	5.9×10^{-3}	[36]
	AgNiO/Alg	0.05	12	5.556×10^{-3}	[37]
	Ag@Cu	0.035	5	6.1×10^{-3}	[38]
	SPDH@Ag-20	0.416	5.42	1.925×10^{-2}	This work
MB	PtAK-1.0	0.078	2	2.73×10^{-3}	[39]
	Pd NPs/CMs	0.025	150	1.9×10^{-4}	[40]
	ZBD@Ag	0.05	6	6.2×10^{-3}	[41]
	SPDH@Ag-20	0.624	14.3	1.371×10^{-2}	This work
MO	Au-Ag BNPs	5	3	9.2×10^{-3}	[42]
	Cu-CC	0.065	3	1.12×10^{-2}	[43]
	Ag/ZIF-7	0.0306	4	1.44×10^{-2}	[44]
	SPDH@Ag-20	0.612	7.3	1.112×10^{-2}	This work

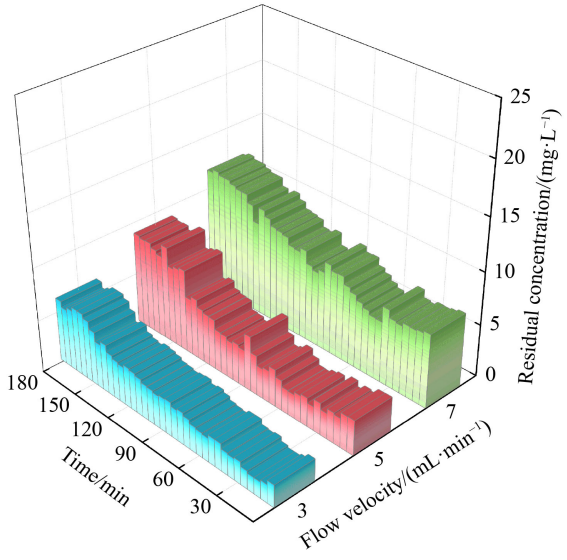

Fig. 9 The results of fixed-bed experiment for SPDH@Ag-20 with different flowing rates: 3, 5, and 7 mL·min^{-1}.

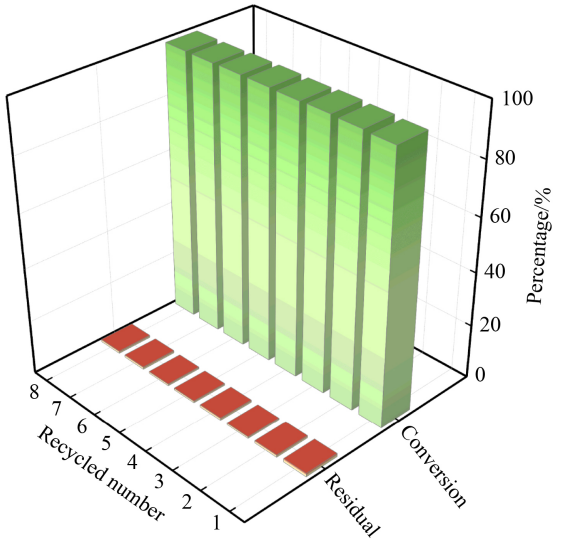

Fig. 10 Conversion percentage and residual rate in 8 cycling tests with SPDH@Ag-20.

3.4 Recyclability and reusability

As a supported catalyst, the macroscopic volume of SPDH@Ag-20 provides outstanding advantages in recycling operations. Figure 10 summarizes the relationship between the conversion percentage and residual rate of 4-NP in eight cycles of the test. The conversion rates of 4-NP were all above 98.7% without a significant decrease after eight repetitions. Figures S6(a) and S6(b) (cf. ESM) are the SEM and TEM images of the recovered SPDH@Ag-20, respectively. It can be seen that the three-dimensional network structure of the composite remains stable, and the Ag NPs have good dispersion on the carrier material without large-area agglomeration. After comparing the SEM-EDS test data of SPDH@Ag-20 before and after the reaction (Tables S3 and S4, cf. ESM), it was found that the change in silver content was slight. In conclusion, SPDH@Ag-20 has good structural stability and catalytic performance in recycling experiments.

Table 2 summarizes related studies in the same field, and the catalytic performance of SPDH@Ag-20 is intuitively exhibited through data comparison. Malik et al. [45] prepared Ag-Fe bimetallic NPs by a simple one-pot method, with a 4-NP conversion of 94.56% in 45 min. By using ZIF-67-Co as a precursor and template, Li et al. [46] prepared a new catalyst that embeds Co NPs in a porous nitrogen-doped carbon framework through pyrolysis. The catalyst had good degradation efficiency, and the reduction of 4-NP was completed within 3 min. Rezaei et al. [47] used covalent organic polymers (COPs) as efficient supports to prepare a non-noble metal catalyst Cu-COP, which converted 4-NP to 4-AP in 3 min and could be reused 5 times. Xu et al. [48] chose a magnetic covalent organic framework (Fe_3O_4@COF) as a carrier material for gold NPs, which showed high catalytic efficiency. More importantly, the magnetic catalyst offers better recyclability. Yu et al. [49] obtained a modified cellulose nanofibril aerogel catalyst (CNF-PEI-1-500) with the Pt NPs size of 2.74 nm by changing the ratio of raw materials. It showed good catalytic activity in the catalytic degradation of 4-NP. Peng et al. [50] used $Ti_3C_2T_x$ (MXene) and AM as raw materials to prepare Ag/MX/PAM hydrogel composite to degrade 4-NP, and the k value was 0.1389 s^{-1}. By comparison, it is found that the catalyst SPDH@Ag-20 prepared in this study has the same catalytic hydrogenation effect.

Table 2 The catalytic performance of SPDH@Ag-20 compared with other reported catalysts

Carrier	Active component	4-NP/ (mmol·L^{-1})	Time/ min	k/s^{-1}	Ref.
Without	Ag-Fe bimetallic NPs	0.2	45	0.001082	[45]
Carbon material	Co	0.1	3	0.0193	[46]
COP	Cu	0.1	3	0.0193	[47]
Fe_3O_4@COF	Au	1.8	24	0.0037	[48]
CNF-PEI-1-500	Pt	15	30	0.00201	[49]
MX/PAM	Ag	0.5	0.5	0.1389	[50]
SPDH	Ag	2	1.88	0.04057	This work

4 Conclusions

In this study, DN hydrogel composites were prepared from SA, AA, and AM as raw materials, which were used as a carrier for the immobilization of silver NPs. Ag NPs were well controlled to generate with uniform size and homogeneous dispersion in hydrogel structure, which was attributed to the dispersing effect of abundant carboxyl and amine groups in SPDH carrier. The optimal loading of silver was found to be 20% through batch experiments. The 4-NP at 5 mmol·L^{-1} was degraded in only 113 s, with a corresponding k value of 0.04157 s^{-1}. In tap water and simulated seawater systems, the conversion rate of 4-NP was also above 99%. Satisfactorily, the conversion remained above 74% after 3 h under fixed bed conditions with a flow rate of 7 mL·min^{-1}. The conversion of 4-NP was maintained at 98.7% in 8 cycles, demonstrating good catalytic stability of SPDH@Ag-20. In addition, SPDH@Ag-20 has been applied to the degradation of multiple dye systems, showing a wide and efficient catalytic performance. As a result, SPDH@Ag has potential industrial applications, and this study provides new ideas for water treatment processes.

Acknowledgements This research was financially supported by the National Natural Science Foundation of China (Grant Nos. 21776026, 22075034, and 22178037), and Liaoning Revitalization Talents Program (Grant Nos. XLYC1902037 and XLYC2002114), and Natural Science Foundation of Liaoning Province of China (Grant No. 2021-MS-303).

Electronic Supplementary Material Supplementary material is available in the online version of this article at https://dx.doi.org/10.1007/s11705-022-2290-8 and is accessible for authorized users.

References

1. Pandey S, Do J Y, Kim J, Kang M. Fast and highly efficient removal of dye from aqueous solution using natural locust bean gum based hydrogels as adsorbent. International Journal of Biological Macromolecules, 2020, 143: 60–75
2. Makhado E, Motshabi B R, Allouss D, Ramohlola K E, Modibane K D, Hato M J, Jugade R M, Shaik F, Pandey S. Development of a ghatti gum/poly (acrylic acid)/TiO_2 hydrogel nanocomposite for malachite green adsorption from aqueous media: statistical optimization using response surface methodology. Chemosphere, 2022, 306: 135524
3. Pandey S, Son N, Kang M. Synergistic sorption performance of karaya gum crosslink poly(acrylamide-co-acrylonitrile)@metal nanoparticle for organic pollutants. International Journal of Biological Macromolecules, 2022, 210: 300–314
4. Pandey S, Mishra S B. Catalytic reduction of *p*-nitrophenol by

using platinum nanoparticles stabilised by guar gum. Carbohydrate Polymers, 2014, 113: 525–531
5. Campos A, Troc N, Cottancin E, Pellarin M, Weissker H C, Lermé J, Kociak M, Hillenkamp M. Plasmonic quantum size effects in silver nanoparticles are dominated by interfaces and local environments. Nature Physics, 2019, 15(3): 275–280
6. Pandey S, Son N, Kim S, Balakrishnan D, Kang M. Locust bean gum-based hydrogels embedded magnetic iron oxide nanoparticles nanocomposite: advanced materials for environmental and energy applications. Environmental Research, 2022, 214(Part 3): 114000
7. Pourmadadi M, Eshaghi M M, Ostovar S, Shamsabadipour A, Safakhah S, Mousavi M S, Rahdar A, Pandey S. UiO-66 metal-organic framework nanoparticles as gifted MOFs to the biomedical application: a comprehensive review. Journal of Drug Delivery Science and Technology, 2022, 76: 103758
8. Kumar A, Sharipov M, Turaev A, Azizov S, Azizov I, Makhado E, Rahdar A, Kumar D, Pandey S. Polymer-based hybrid nanoarchitectures for cancer therapy applications. Polymers, 2022, 14(15): 3027
9. Sharma A, Nagraik R, Sharma S, Sharma G, Pandey S, Azizov S, Chauhan P K, Kumar D. Green synthesis of ZnO nanoparticles using ficus palmata: antioxidant, antibacterial and antidiabetic studies. Results in Chemistry, 2022, 4: 100509
10. Hassanisaadi M, Bonjar A H S, Rahdar A, Varma R S, Ajalli N, Pandey S. Eco-friendly biosynthesis of silver nanoparticles using aloysia citrodora leaf extract and evaluations of their bioactivities. Materials Today. Communications, 2022, 33: 104183
11. Moriai T, Tsukamoto T, Tanabe M, Kambe T, Yamamoto K. Selective hydroperoxygenation of olefins realized by a coinage multimetallic 1-nanometer catalyst. Angewandte Chemie International Edition, 2020, 59(51): 23051–23055
12. Jia W, Tian F, Zhang M, Li X, Ye S, Ma Y, Wang W, Zhang Y, Meng C, Zeng G, Liu J. Nitrogen-doped porous carbon-encapsulated copper composite for efficient reduction of 4-nitrophenol. Journal of Colloid and Interface Science, 2021, 594: 254–264
13. Hussain I, Shahid M, Ali F, Irfan A, Begum R, Farooqi Z H. Polymer hydrogels for stabilization of inorganic nanoparticles and their application in catalysis for degradation of toxic chemicals. Environmental Technology, 2021, 42(1): 1–11
14. Farooqi Z H, Sultana H, Begum R, Usman M, Ajmal M, Nisar J, Irfan A, Azam M. Catalytic degradation of malachite green using a crosslinked colloidal polymeric system loaded with silver nanoparticles. International Journal of Environmental Analytical Chemistry, 2022, 102(16): 4104–4120
15. Hussain I, Farooqi Z H, Ali F, Begum R, Irfan A, Wu W, Wang X, Shahid M, Nisar J. Poly(styrene@N-isopropylmethacrylamide-co-methacrylic acid)@Ag hybrid particles with excellent catalytic potential. Journal of Molecular Liquids, 2021, 335: 116106
16. Shah L A, Haleem A, Sayed M, Siddiq M. Synthesis of sensitive hybrid polymer microgels for catalytic reduction of organic pollutants. Journal of Environmental Chemical Engineering, 2016, 4(3): 3492–3497
17. Wang L, Chen S, Zhou J, Yang J, Chen X, Ji Y, Liu X, Zha L. Silver nanoparticles loaded thermoresponsive hybrid nanofibrous hydrogel as a recyclable dip-catalyst with temperature-tunable catalytic activity. Macromolecular Materials and Engineering, 2017, 302(10): 1700181
18. Khan M, Shah L A, Khan M A, Khattak N S, Zhao H. Synthesis of an un-modified gum arabic and acrylic acid based physically cross-linked hydrogels with high mechanical, self-sustainable and self-healable performance. Materials Science and Engineering C, 2020, 116: 111278
19. Zhang X, Zhang Y, Zhang W, Dai Y, Xia F. Gold nanoparticles-deranged double network for janus adhesive-tough hydrogel as strain sensor. Chemical Engineering Journal, 2021, 420(Part 3): 130447
20. Khan M, Shah L A, Rahman T U, Yoo H M, Ye D, Vacharasin J. Hydrophobically associated functionalized CNT-reinforced double-network hydrogels as advanced flexible strain sensors. ACS Applied Polymer Materials, 2022, 4(10): 7397–7407
21. Subhan H, Alam S, Shah L A, Khattak N S, Zekker I. Sodium alginate grafted hydrogel for adsorption of methylene green and use of the waste as an adsorbent for the separation of emulsified oil. Journal of Water Process Engineering, 2022, 46: 102546
22. Wu D, Yi M, Duan H, Xu J, Wang Q. Tough TiO_2-rGO-PDMAA nanocomposite hydrogel via one-pot UV polymerization and reduction for photodegradation of methylene blue. Carbon, 2016, 108: 394–403
23. He X, Gopinath K, Sathishkumar G, Guo L, Zhang K, Lu Z, Li C, Kang E T, Xu L. UV-assisted deposition of antibacterial Ag-tannic acid nanocomposite coating. ACS Applied Materials & Interfaces, 2021, 13(17): 20708–20717
24. Gao C, An Q, Xiao Z, Zhai S, Zhai B, Shi Z. Alginate and polyethyleneimine dually mediated synthesis of nanosilver-containing composites for efficient *p*-nitrophenol reduction. Carbohydrate Polymers, 2018, 181: 744–751
25. Makhado E, Pandey S, Modibane K D, Kang M, Hato M J. Sequestration of methylene blue dye using sodium alginate poly(acrylic acid)@ZnO hydrogel nanocomposite: kinetic, isotherm, and thermodynamic investigations. International Journal of Biological Macromolecules, 2020, 162: 60–73
26. Wang Z, Peng X, Guo S, Sun M, Cheng J, Zou L, Chi B, Pu J. Ultraviolet light-assisted $Ag@La_{0.6}Sr_{0.4}Fe_{0.9}Mn_{0.1}O_3$ nanohybrids: a facile and versatile method for preparation of highly stable catalysts in $Li-O_2$ batteries. ACS Applied Energy Materials, 2021, 4(9): 9376–9383
27. Zhang Z, Hu J, Wang Y, Shi R, Ma Y, Huang H, Wang H, Wei J, Yu Q. Relationship between microstructure of AgCl film and electrochemical behavior of Ag|AgCl electrode for chloride detection. Corrosion Science, 2021, 184: 109393
28. Nguyen T T N, Lee M S. Purification of the sodium hydroxide leaching solution of black dross by removal of silicate(IV) with polyacrylamide (PAM). Mineral Processing and Extractive Metallurgy Review, 2021, 42(1): 9–16
29. Ryu J H, Han N K, Lee J S, Jeong Y G. Microstructure, thermal and mechanical properties of composite films based on carboxymethylated nanocellulose and polyacrylamide. Carbohydrate Polymers, 2019, 211: 84–90
30. Xu S, Liang W, Xu G, Huang C, Zhang J, Lang M. A fast and dual crosslinking hydrogel based on vinyl ether sodium alginate.

Applied Surface Science, 2020, 515: 145811
31. Das R, Sypu V S, Paumo H K, Bhaumik M, Maharaj V, Maity A. Silver decorated magnetic nanocomposite (Fe_3O_4@PPy-MAA/Ag) as highly active catalyst towards reduction of 4-nitrophenol and toxic organic dyes. Applied Catalysis B: Environmental, 2019, 244: 546–558
32. Dong G, Cao Y, Zheng S, Zhou J, Li W, Zaera F, Zhou X. Catalyst consisting of Ag nanoparticles anchored on amine-derivatized mesoporous silica nanospheres for the selective hydrogenation of dimethyl oxalate to methyl glycolate. Journal of Catalysis, 2020, 391: 155–162
33. e T, Ma D, Yang S, Hao X, 0. Ma D, Yang S, Hao X. Graphene oxide-montmorillonite/sodium alginate aerogel beads for selective adsorption of methylene blue in wastewater. Journal of Alloys and Compounds, 2020, 832: 154833
34. Gao C, Xiao L, Zhou J, Wang H, Zhai S, An Q. Immobilization of nanosilver onto glycine modified lignin hydrogel composites for highly efficient *p*-nitrophenol hydrogenation. Chemical Engineering Journal, 2021, 403: 126370
35. Shah L A. Developing Ag-tercopolymer microgels for the catalytic reduction of *p*-nitrophenol and Eosin Y throughout the entire pH range. Journal of Molecular Liquids, 2019, 288: 111045
36. Yan Q, Wang X Y, Feng J J, Mei L P, Wang A J. Simple fabrication of bimetallic platinum-rhodium alloyed nano-multipods: a highly effective and recyclable catalyst for reduction of 4-nitrophenol and rhodamine B. Journal of Colloid and Interface Science, 2021, 582(Part B): 701–710
37. Khalil A, Ali N, Asiri A M, Kamal T, Khan S B, Ali J. Synthesis and catalytic evaluation of silver@nickel oxide and alginate biopolymer nanocomposite hydrogel beads. Cellulose, 2021, 28(18): 11299–11313
38. Khan Z, Bashir O, Khan M N, Khan T A, Al-Thabaiti S A. Cationic surfactant assisted morphology of Ag@Cu, and their catalytic reductive degradation of rhodamine B. Journal of Molecular Liquids, 2017, 248: 1096–1108
39. Subhan F, Aslam S, Yan Z, Yaseen M, Zada A, Ikram M. Fabrication of highly dispersed Pt NPs in nanoconfined spaces of as-made KIT-6 for nitrophenol and MB catalytic reduction in water. Separation and Purification Technology, 2021, 265: 118532
40. Yu Y, Liu S, Pei Y, Luo X. Growing Pd NPs on cellulose microspheres via *in-situ* reduction for catalytic decolorization of methylene blue. International Journal of Biological Macromolecules, 2021, 166: 1419–1428
41. Lajevardi A, Tavakkoli Yaraki M, Masjedi A, Nouri A, Hossaini Sadr M. Green synthesis of MOF@Ag nanocomposites for catalytic reduction of methylene blue. Journal of Molecular Liquids, 2019, 276: 371–378
42. Akilandaeaswari B, Muthu K. One-pot green synthesis of Au−Ag bimetallic nanoparticles from lawsonia inermis seed extract and its catalytic reduction of environmental polluted methyl orange and 4-nitrophenol. Journal of the Taiwan Institute of Chemical Engineers, 2021, 127: 292–301
43. Khan S B, Khan M S J, Kamal T, Asiri A M, Bakhsh E M. Polymer supported metallic nanoparticles as a solid catalyst for the removal of organic pollutants. Cellulose, 2020, 27(10): 5907–5921
44. Malik A, Nath M. Synthesis of Ag/ZIF-7 by immobilization of Ag nanoparticles onto ZIF-7 microcrystals: a heterogeneous catalyst for the reduction of nitroaromatic compounds and organic dyes. Journal of Environmental Chemical Engineering, 2020, 8(6): 104547
45. Malik M A, Alshehri A A, Patel R. Facile one-pot green synthesis of Ag−Fe bimetallic nanoparticles and their catalytic capability for 4-nitrophenol reduction. Journal of Materials Research and Technology, 2021, 12: 455–470
46. Li X, Zeng C, Jiang J, Ai L. Magnetic cobalt nanoparticles embedded in hierarchically porous nitrogen-doped carbon frameworks for highly efficient and well-recyclable catalysis. Journal of Materials Chemistry A: Materials for Energy and Sustainability, 2016, 4(19): 7476–7482
47. Rezaei F, Dinari M. Cu nanoparticles embedded in the porous organic polymer as highly effective catalysts for nitroaromatics reduction. Microporous and Mesoporous Materials, 2021, 325: 111339
48. Xu Y, Shi X, Hua R, Zhang R, Yao Y, Zhao B, Liu T, Zheng J, Lu G. Remarkably catalytic activity in reduction of 4-nitrophenol and methylene blue by Fe_3O_4@COF supported noble metal nanoparticles. Applied Catalysis B: Environmental, 2020, 260: 118142
49. Yu H, Oh S, Han Y, Lee S, Jeong H S, Hong H J. Modified cellulose nanofibril aerogel: tunable catalyst support for treatment of 4-nitrophenol from wastewater. Chemosphere, 2021, 285: 131448
50. Peng C, Kuai Z, Li X, Lian S, Jiang D, Tang J, Li L, Wu R, Wu A, Chen S. Facile synthesis of Ag nanoparticles/$Ti_3C_2T_x$/polyacrylamide composite hydrogel as efficient catalyst for methylene blue and 4-nitrophenol reduction. Materials & Design, 2021, 210: 110061